ARTICLE

Check for updates

Magnonic Klein and acausal tunneling enabled by breaking the anti parity-time symmetry in antiferromagnets

Shaohua Yuan[1], Chaowei Sui[1], Zhengduo Fan[1], Jamal Berakdar [2✉], Desheng Xue[1] & Chenglong Jia [1,3✉]

Klein tunneling associated with particle-antiparticle pair productions across a potential barrier is a key prediction of quantum-field theory for relativistic particles. Yet, a direct experimental realization is hampered by the particles large rest mass resulting in high potential barrier. Here, for non-Hermitian antiferromagnets, at the verge of the anti-parity-time symmetry transition, chiral magnons are demonstrated to offer a bosonic platform to access Klein tunneling at meV energies in experimentally feasible settings. Our analytical and numerical simulations evidence that magnetic damping renders a low energy mechanism for the breakdown of the magnonic vacuum and for creating particle-antiparticle pairs in strong magnetic fields. Adopting Feynman's picture for antiparticles, the tunneling time of an incident magnon wave packet across a supercritical barrier is found to be negative. The uncovered aspects point to the potential of chiral magnons for addressing fundamental physics in a conceptually simple setup with the potential for use in chirality-dependent magnonic computing.

[1] Key Laboratory for Magnetism and Magnetic Materials of the Ministry of Education, Lanzhou University, Lanzhou, China. [2] Institut für Physik, Martin-Luther-Universität Halle-Wittenberg, Karl-Freiherr-von-Fritsch-Strasse 3, Halle 06120 SA, Germany. [3] Lanzhou Center for Theoretical Physics & Key Laboratory of Quantum Theory and Applications of MOE, Lanzhou University, Lanzhou, China. ✉email: jamal.berakdar@physik.uni-halle.de; cljia@lzu.edu.cn

A spontaneous breaking of a continuous symmetry entails the presence of massless (zero-energy) modes, meaning the mode energies $\omega(\mathbf{k})$ vanish, as the wavevector $\mathbf{k}$ tends to zero (Goldstone theorem)[1,2]. Such Goldstone modes appear in spin systems with spin rotation symmetry in the long wavelength limit as spin waves (SWs) with magnons being the excitation quanta[3,4]. The presence of interactions not compatible with spin rotation symmetry may lead to damping of the spin excitations. Thus, the effective low-energy Hamiltonian describing SWs is generally not Hermitian and may exhibit non-Hermitian degeneracies (called exceptional points, EPs)[5]. For ferromagnets (FM) with a single magnetic lattice, SWs are always right-handed circularly polarized[6,7]. For antiferromagnets (AFM) in G-type ordering $\mathbf{m}(\mathbf{r})$ or for synthetic AFM (SyAFM), meaning metal-spacer-separated two magnetic layers with antiparallel spins[8,9], a translation with a lattice vector $\mathbf{a}$ between the two magnetic sublattices (e.g., sublattice A for spin-up and sublattice B for spin-down) implies $\mathbf{m}(\mathbf{r}+\mathbf{a}) \rightarrow -\mathbf{m}(\mathbf{r})$. In this case the SW Hamiltonian is shown to be in general anti-parity-time (anti-$\mathcal{PT}$) symmetric and non-Hermitian[10]. In addition to the spin rotation symmetry break, a breaking of the anti-$\mathcal{PT}$ symmetry may occur and is signaled by the emergence of EP and chiral magnons. For instance, this symmetry break can be brought about by increasing the local magnetic damping and/or the AFM interaction strength between the two sublattices (Fig. 1). In anti-$\mathcal{PT}$ symmetry-preserved (APT) phase, the spin excitations in the two sublattices are equator modes with a maximally coherent superposition, no spin waves are radiated. In anti-$\mathcal{PT}$ symmetry-broken (APTB) phase, the two types of magnons with opposite chirality (right-handed or left-handed) are dominated by the spin precession in the sublattice A or B, respectively[11,12]. This chirality, as a new degree of freedom, is akin to AFM magnons and may serve to encode information[13–16]. General aspects of $\mathcal{PT}$ and anti-$\mathcal{PT}$ symmetry in magnetic excitations have been discussed recently, for instance in[10,17–21]. Here, we are interested in consequences thereof on the magnon scattering characteristics.

From an energy point of view, right-handed and left-handed AFM magnons possess respectively positive and negative dispersion (real part of eigenfrequencies) and can be viewed as particles and antiparticles. Therefore, similar to chiral fermions in graphene[22], a magnonic setup based on AFM bipartite lattices can be constructed to test for relativistic effects[23–30].

Here, we demonstrate that Klein paradox, entailing chiral magnon-pair productions and acausal tunneling, can be realized by scattering from a step potential for magnons caused by spatio-temporally varying magnetic fields. Within the region of a strong field, we find that the imaginary eigenfrequency of the antiparticle magnon states is shifted up becoming positive which is signaled by an enhanced density of a left-handed magnon wave packet. Feynman's picture of antiparticle as being particle moving backward in time[31], is used for the interpretation of the acausal magnonic transmission mechanism across a supercritical barrier by Klein tunneling. The results are generic and not limited to G-type AFMs with the Dirac spectrum but also in SyAFMs described by coupled Schrödinger equations. Our finding points to the importance of chirality rather than the linear dispersion for Klein tunneling, and to chiral magnons in AFM as a versatile platform for experimentally elucidating fundamental physics at low energies (~meV) and at mesoscopic length scale.

Results and discussion

Anti-$\mathcal{PT}$ symmetric AFM dynamics. We study SW excitations in a SyAFM consisting of two FM sublayers with the normalized magnetization vector fields $\mathbf{m}_n$ ($n = 1, \bar{1}$) (the analysis and results for the case of G-type AFMs can be found in the Supplementary Note 3). SWs can be described by linearizing the Landau-Lifshitz-Gilbert (LLG) equations[10]

$$\partial_t \mathbf{m}_n = -\frac{\gamma_n}{1+\alpha_n^2} \mathbf{m}_n \times \left[\mathbf{H}_n^{\text{eff}} + \alpha_n(\mathbf{m}_n \times \mathbf{H}_n^{\text{eff}})\right]. \quad (1)$$

γ_n (α_n) is the gyromagnetic ratio (Gilbert damping). The effective magnetic field

$$\mathbf{H}_n^{\text{eff}} = 2(\mathcal{A}_n \nabla^2 \mathbf{m}_n + \mathcal{K}_z m_n^z \hat{e}_z - J\mathbf{m}_{\bar{n}}), \quad (2)$$

depends on the Heisenberg exchange coupling $\mathcal{A}_n$ between neighboring sites within the n-layer, the magnetic anisotropy $\mathcal{K}_z$ along the easy axis (taken as the z-axis), and the Ruderman-Kittel-Kasuya-Yosida (RKKY) interaction J between the two FM
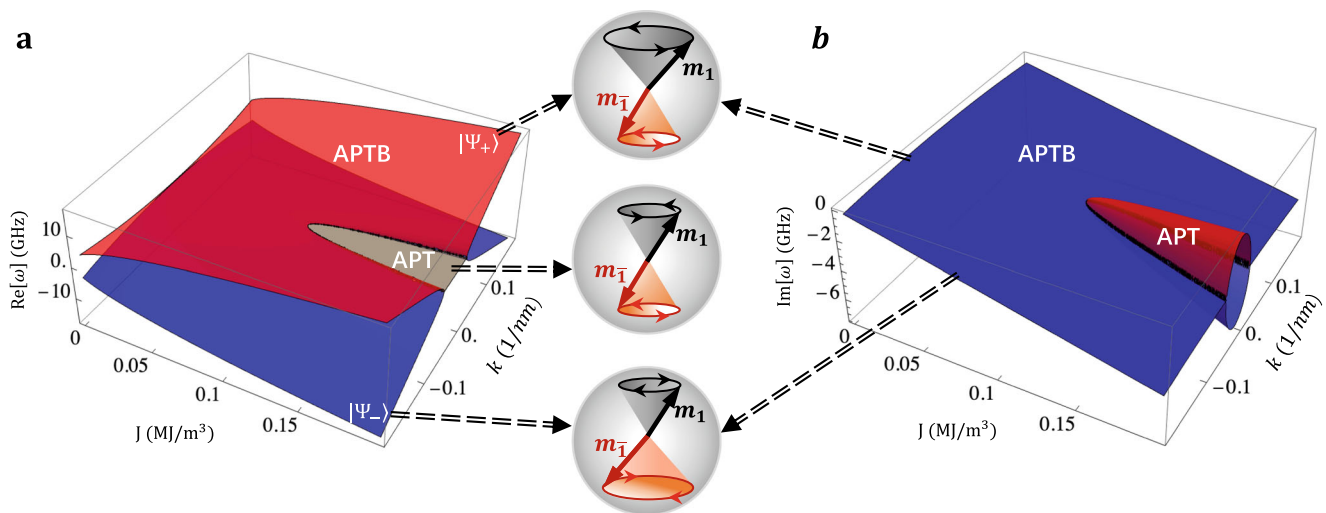
Fig. 1 Magnons in synthetic antiferromagnets governed by anti-$\mathcal{PT}$ symmetric Hamiltonian. a Real and **b** imaginary part of the dispersion $\omega(k)$ as a function of the antiferromagnetic (AFM) interaction J. In the anti-$\mathcal{PT}$ symmetry-preserved (APT) phase, the spin dynamics in the two magnetic sublayers (m_1 and $m_{\bar{1}}$) share the same amplitude, no preferred chirality and no net polarization are induced. In the anti-$\mathcal{PT}$ symmetry-broken (APTB) phase, the appearance of right- and left-handed modes, $|\Psi_\pm\rangle$ with negative/positive polarization-charge signals a break of the anti-$\mathcal{PT}$ symmetry. Note that $\text{Im}[\omega] \leq 0$ holds in both APT (red) and APTB (blue) phases. In both phases the stable vacuum state is the Néel state to which all excitation decays in presence of Gilbert damping. Other parameters are: exchange stiffness $\mathcal{A} = 0.4$ pJ m^{-1}, uniaxial magnetic anisotropy $\mathcal{K}_z = 0.5$ kJ m^{-3}, and Gilbert damping $\alpha = 0.1$.

sublayers[32,33]. We assume $J > 0$ and a large enough $\mathcal{K}_z$ to suppress quantum fluctuations enforcing so a collinear antiferromagnetic (Néel) equilibrium configuration aligned along the easy axis. SWs are collective small transversal fluctuations $\mathbf{m}_n^\perp$ around the Néel ground state: $\mathbf{m}_n = m_n^z \hat{e}_z + \mathbf{m}_n^\perp$ with $m_1^z \approx -m_{\bar{1}}^z \approx 1$ and $\|\mathbf{m}_n^\perp\| \ll 1$.

To expose the chirality of SWs, we introduce two complex variables $\Psi(\mathbf{r}, t) = (\psi_1, \psi_{\bar{1}})^{\mathrm{T}}$ and $\Phi(\mathbf{r}, t) = (\phi_1, \phi_{\bar{1}})^{\mathrm{T}}$ with

$$\psi_n = m_n^x - i m_n^y \text{ and } \phi_n = m_n^x + i m_n^y. \tag{3}$$

We note that ψ_n and $\psi_{\bar{n}}$ are distinguished by the Pauli matrix σ_i in the sublattice space, while ψ_n and ϕ_n can be distinguished by τ_i in isospin space[34], thus the basis elements (3) are independent. For the fully symmetric case, meaning in the event that in Eqs. (1), (2) $\mathcal{A}_1 = \mathcal{A}_{\bar{1}} = \mathcal{A}$, $\tilde{\gamma}_n = \frac{2\gamma_n}{1+\alpha_n^2} = \gamma$, and $\tilde{\alpha}_n = \frac{2\alpha_n \gamma_n}{1+\alpha_n^2} = \alpha$, and to a linear order in $\|\mathbf{m}_n^\perp\|$, one infers that the SW dynamics obeys the equation of motion

$$i\partial_t \begin{bmatrix} \Psi(\mathbf{r}, t) \\ \Phi(\mathbf{r}, t) \end{bmatrix} = \begin{bmatrix} \mathcal{H} & 0 \\ 0 & -\mathcal{H}^\star \end{bmatrix} \begin{bmatrix} \Psi(\mathbf{r}, t) \\ \Phi(\mathbf{r}, t) \end{bmatrix} \tag{4}$$

where the Schrödinger-type Hamiltonian $\mathcal{H}$ in a plane-wave basis $\psi_n(\phi_n) \sim e^{i\mathbf{k}\cdot\mathbf{r}-i\omega t}$ (appropriate in the long-wavelength limit) reads

$$\mathcal{H} = \begin{bmatrix} E_k(1-i\alpha) & J(1-i\alpha) \\ -J(1+i\alpha) & -E_k(1+i\alpha) \end{bmatrix} \tag{5}$$

with $E_k = \mathcal{A}\mathbf{k}^2 + \mathcal{K}_z + J$.

A parity operation $\hat{\mathcal{P}}$ with respect to sublattice exchange is realized by the Pauli operator σ_x. The time-reversal operation $\hat{\mathcal{T}}$ results in $i \to -i$, $t \to -t$ and $\mathbf{k} \to -\mathbf{k}$. Therefore, we find

$$\hat{\mathcal{P}}\hat{\mathcal{T}}\mathcal{H} = -\mathcal{H}\hat{\mathcal{P}}\hat{\mathcal{T}}. \tag{6}$$

So, $\mathcal{H}$ is anti-$\mathcal{PT}$ symmetric. The eigenvalues of $\mathcal{H}$ are

$$\omega_\pm = E_k\left(-i\alpha \pm \sqrt{1-\xi_k^2}\right), \tag{7}$$

with $\xi_k = J\sqrt{1+\alpha^2}/E_k$. The corresponding eigenvectors are

$$\Psi_+ = \begin{pmatrix} \cosh\frac{\theta}{2} \\ -\sinh\frac{\theta}{2}e^{i\varphi} \end{pmatrix}, \quad \Psi_- = \begin{pmatrix} -\sinh\frac{\theta}{2} \\ \cosh\frac{\theta}{2}e^{i\varphi} \end{pmatrix}, \tag{8}$$

with $\tan\varphi = \alpha$ and $\tanh\theta = \xi_k$. Equation (7) indicates the emergence of an exceptional point (EP) at $\|\xi_k\| = 1$, separating the APT phase-space region with purely imaginary eigenfrequencies and the APTB phase with complex eigenfrequencies, as shown in Fig. 1. The system can be driven across the phase transition by varying J, $\mathcal{K}_z$ and/or α. Clearly, for isotropic SyAFMs with the anisotropy $\mathcal{K}_z = 0$ we can have $\xi_k > 1$ when E_k is around its minimum at $|k| = 0$.

In the APT phase as $\xi_k > 1$, $\Psi_\pm$ are also eigenvectors of the $\hat{\mathcal{P}}\hat{\mathcal{T}}$ operator satisfying

$$\hat{\mathcal{P}}\hat{\mathcal{T}}\Psi_\pm = \lambda_\pm \Psi_\pm \text{ with } \|\lambda_\pm\|^2 = 1. \tag{9}$$

The dynamic motions of $\mathbf{m}_1$ and $\mathbf{m}_{\bar{1}}$ in the two coupled FM sublayers are modes with $\|\psi_1\| = \|\psi_{\bar{1}}\|$. The system remains magnetically neutral in the dynamic states and no net spin polarization is generated by spin excitations. Within the APT phase, low-energy magnetization excitations decays exponentially with time and can not be efficiently radiated in the form of spin waves. Note that for both APT and APTB phases we start from the stable (vacuum) Néel state, and excitations relax eventually (due to Gilbert damping) to the stable vacuum.

The characteristics of the eigenmodes $\Psi_\pm$ change qualitatively as soon as $\xi_k < 1$, in which case the system enters the APTB phase with complex $\omega_\pm$. Analysis of the eigenvectors shows that Ψ_+

(Ψ_-) with $\mathrm{Re}[\omega_+] > 0$ ($\mathrm{Re}[\omega_-] < 0$) is a right-handed (left-handed) precession of the Néel vector $\mathbf{n} = (\mathbf{m}_1 - \mathbf{m}_{\bar{1}})/2$. As sketched in Fig. 1a, b, the modes $\Psi_\pm$ with opposite chirality are dominated by precession in different sublayer. That is, Ψ_+ with $\|\psi_1\| > \|\psi_{\bar{1}}\|$ while Ψ_- with $\|\psi_1\| < \|\psi_{\bar{1}}\|$, which results in a small opposite circular-polarization (i.e., net magnetization) $\mathbf{p} = (\langle\mathbf{m}_1\rangle + \langle\mathbf{m}_{\bar{1}}\rangle)/2$ along the z-direction, namely, negative (positive) polarization-charge p_z for right-handed (left-handed) $\Psi_\pm$ magnons, respectively. Therefore, the emergent net magnetization may serve to trace the breaking of the anti-$\mathcal{PT}$ symmetry of chiral magnon excitations in AFMs. Experimentally, the realization of electrically tunable RKKY interactions (J) has been reported[32,33]. Via interfacial magnetoelectric couplings, the magnetic anisotropy $\mathcal{K}_z$ and effective magnetization damping α can be tuned by gate voltage as well. By scanning these parameters, the anti-PT phase transition can be observed in SyAFMs.

Particle-hole symmetry of AFM magnons. The anti-$\mathcal{PT}$ symmetry breaking holds true for the complex conjugate $\Phi(\mathbf{r}, t)$ as well. However, the eigenmode Φ_+ having $\mathrm{Re}(\omega_+) > 0$ corresponds to the left-handed magnons with a positive polarization-charge ($p_z > 0$), and the negative frequency mode Φ_- corresponds to the right-handed mode with a negative polarization-charge ($p_z < 0$). Therefore, we can take two degenerated states, for instance Ψ_+ and Φ_+, as the isospin basis for AFM magnons, where magnon states in the isospin space have same frequencies but opposite isospin (chirality) and opposite polarization-charge. Similar to relativistic fermions, we have so four well-defined magnon states, $\Psi_\pm$ and $\Phi_\pm$ in AFM systems in the APTB phase.

In the sublattice space the $\Psi_\pm$ magnons with positive/negative energies have particle-hole symmetry and live on the hyperboloid of two sheets SU(1,1). In addition, the SyAFM Hamiltonian is invariant under global spin rotation around the easy z-axis. Thus, the z-component of the total spin is a good quantum number. Consequently, $\mathcal{H}$ with zero damping ($\alpha = 0$) is pseudo-Hermitian, $\mathcal{H}^\dagger = \sigma_z \mathcal{H}\sigma_z$, and the total polarization-charge density $N_z = \int d\mathbf{r}\rho(\mathbf{r}, t)$ in the sublattice space is conserved, where $\rho(\mathbf{r}, t) = \Psi^\dagger \sigma_z \Psi$. The conserved N_z helps identifying the magnonic Klein paradox with particle-antiparticle (P-AP) pair productions. For a finite magnetic damping, we have $\mathrm{Im}[\omega_\pm] < 0$ (Fig. 1b) and a time-decaying polarization-charge density. The larger is the rest mass m of magnons ($m^2 = [\mathcal{K}_z(\mathcal{K}_z + 2J)] - J^2\alpha^2$), the faster the P-AP ($\Psi_+$-$\Psi_-$) pair decays into the magnonic vacuum (Néel state). Clearly, the above arguments apply to Φ_+-Φ_- pairs.

Magnetic field effects on AFM magnons. To elucidate the nature of the magnonic P-AP pairs, we separate the Ψ-branch from the Φ-branch magnons. The degeneracy in the isospin space is protected by the combined $\mathcal{PT}$ symmetry of AFM systems. Therefore, we apply a normal magnetic field ($\mathbf{B} = B_z\hat{e}_z$) breaking the time-reversal symmetry and lifting the two-fold isospin degeneracy of AFM magnons (see Supplementary Note 1) but it does not affect the stability of the vacuum. Starting from the collinear Néel state, $\mathcal{H}$ turns non-Hermitian with a *passive* anti-$\mathcal{PT}$ symmetry,

$$\mathcal{H} = \begin{bmatrix} (E_k + B_z)(1-i\alpha) & J(1-i\alpha) \\ -J(1+i\alpha) & -(E_k - B_z)(1+i\alpha) \end{bmatrix}. \tag{10}$$

Figure 2 demonstrates the usefulness of the linearized model by comparing to the results of the full numerical simulations of the LLG Eq. (1). As shown in Fig. 2c, energies of $\Psi_\pm$ magnon states are shifted up but those of the $\Phi_\pm$ states are lowered upon applying a magnetic field. In other words, B_z tunes to the favorable regime for characterizing magnon transport in that, the
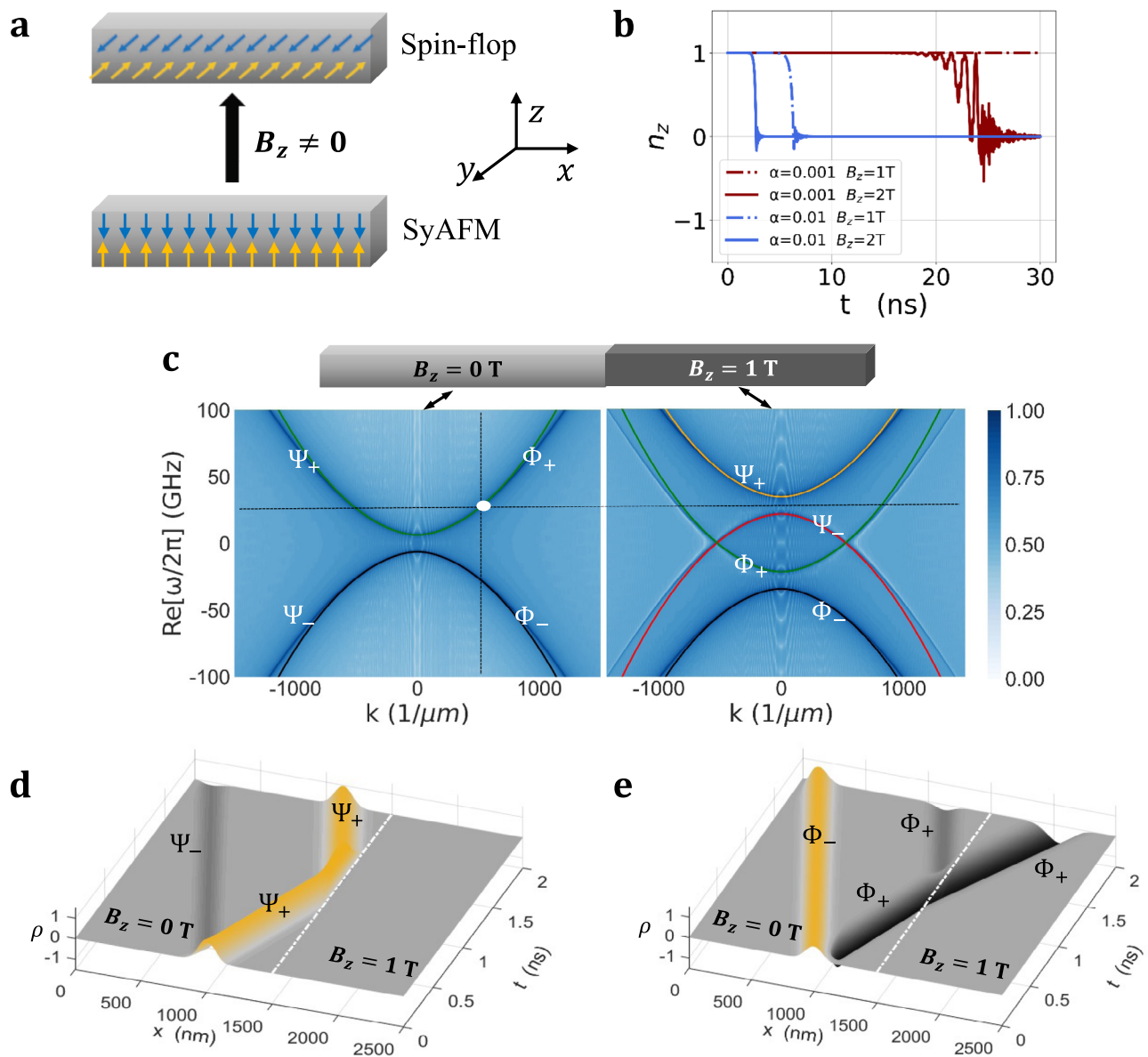
Fig. 2 Chiral tunneling of antiferromagnetic (AFM) magnons through a potential step. a Schematic spin-flop transition in synthetic antiferromagnets (SyAFMs) induced by applied normal magnetic fields when $J > \mathcal{K}_z$. **b** Spin-flop time of the Néel vector component n_z in dependence of the Gilbert damping α in the presence of different magnetic fields $\mathbf{B}_z$ at zero temperature (detailed quantifications of the effects of elevated temperatures are enclosed in the Supplementary Note 4). **c** Density plots of the energy dispersion relation under magnetic field pulses with $B_z = 0$ T and $B_z = 1$ T, respectively. They are obtained from the normalized Fast Fourier Transform (FFT) intensities (quantified by the colour bar) that follow from full micromagnetic simulations of the Landau-Lifshitz-Gilbert (LLG) equations. The analytical eigen-frequencies of four spin-wave eigenmodes ($\Psi_\pm$ and $\Phi_\pm$) are shown by the solid curves. Importantly, the pulse duration is shorter than the corresponding spin-flop time in **b**. **d, e** Time evolution of incoming Ψ_+ and Φ_+ wave packets with the center momentum $k_0 = 500\ \mu m^{-1}$. Correspondingly, the incident center frequency $\omega(k_0)$ is located in the lifted-up energy gap between the $\Psi_\pm$ magnons, as marked by the white dot and black dashed lines. By increasing the potential step or lowering the incident energy, the Klein paradox occurs. In all figures the polarization charge density ρ is renormalized by the initial incident wave packet (WP) for comparison. In the simulations, we assumed for saturation magnetization $M_s = 8.0 \times 10^5$ A m^{-1}, exchange stiffness $\mathcal{A} = 1.0$ pJ m^{-1}, uniaxial magnetic anisotropy $\mathcal{K}_z = 35$ kJ m^{-3}, and the inter-sublayer AFM coupling between two ferromagnetic (FM) sublayers is $\sigma = -10^{-4}$ J m^{-2} (the energy density of Ruderman-Kittel-Kasuya-Yosida (RKKY) interaction is $J = -\sigma/a$ with a being the lattice constant).

spatio-temporal character of B_z is reflected in a corresponding spatio-temporal shape of an emergent potential barrier (well) for $\Psi_\pm$ ($\Phi_\pm$) magnons having a positive (negative) isospin.

However, a strong external magnetic field may destabilize the initial Néel ground state along the easy axis[35]. For instance, a large field may result in a spin-flop transition[36,37], where antiparallel spins $\mathbf{m}_1$ and $\mathbf{m}_{\bar{1}}$ are approximately perpendicular to the external field **B** as to minimize the total energy (Fig. 2a).

We performed numerical micromagnetic simulations under initial collinear Néel ordering along the easy z-axis (technical details and parameter values of the simulations are referred to the Methods) and find that the spin-flop time τ_{sf} depends inversely on the damping parameter α, i.e. $\tau_{sf} \propto 1/\alpha$[38]. For SyAFMs with small Gilbert damping, τ_{sf} can be over several tens of nanoseconds at low enough temperatures (Fig. 2b and the discussion of the temperature effects in the Supplementary
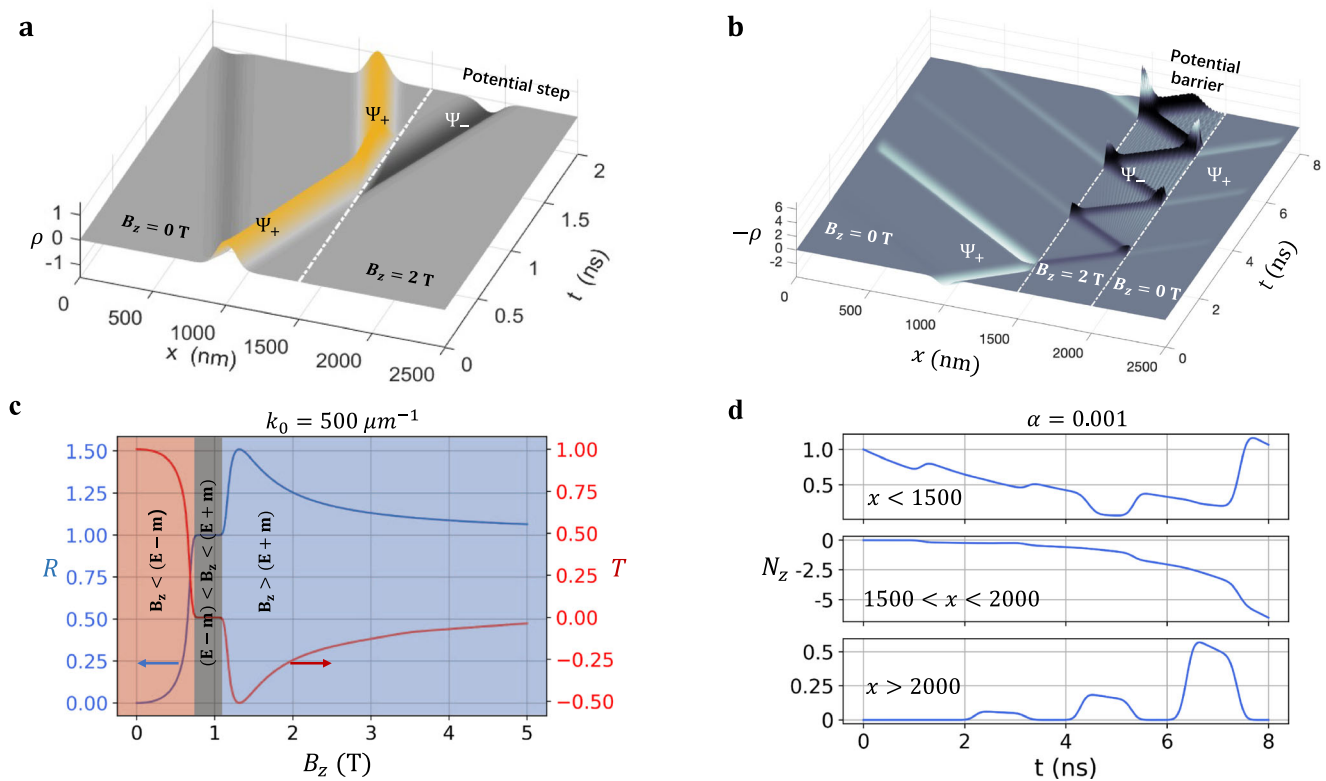
Fig. 3 Klein paradox and particle-antiparticle (P-AP) pair productions of synthetic antiferromagnetic (SyAFM) magnons. Scattering of the incident Ψ_+ wave packets with the central wave vector $k_0 = 500 \mu m^{-1}$ by **a** the Klein step and **b** the supercritical square barrier induced by a space-varying magnetic field pulse $B_z = 2$ T. Abundance of Ψ_+-Ψ_- pairs are produced upon reflection at the barrier's edges. **c** Reflection (R) and transmission (T) coefficients of the Ψ_+ wave packet by the potential step as a function of the applied magnetic fields B_z. Note that $\alpha = 0$ is used during the simulations to validate $R + T = 1$. **d** Time evolution of the total polarization-charge in the left ($x < 1500$ nm), interior ($1500 < x < 2000$ nm), and right ($x > 2000$ nm) regions across the supercritical square barrier. Now, the finite Gilbert damping $\alpha = 0.001$ is used. In all simulations the incoming center energy of the Ψ_+ wave packet is $E = \omega(k_0)$. The simulation parameters are the same as in Fig. 2.

Note 4). The time evolution of magnons in question proceeds on the order of nanoseconds (the tunneling time is less than 2 ns as shown in Figs. 2 and 3). During this time the initial Néel order is maintained and in the meantime the SW excitations are described well by the Hamiltonian, Eq. (10) (Fig. 2c and Supplementary Note 3). The time window is thus large enough to investigate the magnon scattering off the potential step generated by a local magnetic field.

Chiral tunneling. We study at first the transmission properties of the Ψ and Φ branch magnons. The incident magnonic wave packet (WP) is chosen as the Gaussian $Ae^{-(x-x_0)^2/L^2}e^{i(k_0 x + \theta)}(1,0)^T$ starting at x_0 with amplitude $A = 0.001$ and $L^2 = 8000$ nm^2. In the region with zero magnetic field, the Ψ_+ and Φ_+ WPs can be launched by choosing negative/positive k_0 or different phases, $\theta = 0$ or $\theta = -\pi/2$, respectively. As shown in Fig. 2 d, e, the initial WPs at $x_0 = 1000$ nm split immediately into two parts: antiparticle (Ψ_-/Φ_-) waves move left (with negative energy) while the particle (Ψ_+/Φ_+) waves move right (with positive energy). After around 1 ns, the right moving magnons reach the left edge of the step potential due to the applied, normal magnetic field $B_z = 1$ T for $x \geq 1500$ nm. Since the incoming center frequency $\omega(k_0)$ is now in the lifted energy gap between $\Psi_{\pm}$ eigenmodes, the Ψ_+ magnons are subject to a potential step but the Φ_+ magnons experience a potential well. As a result, Ψ_+ magnons are totally reflected but Φ_+ magnons do mostly transmit across the step edge. In other words, a chiral tunneling of AFM magnons is realized: we have a magnonic insulator (metal) to the incident Ψ_+ (Φ_+) magnons by adjusting the amplitude of applied magnetic

field with respect to the center frequency $\omega(k_0)$ of the incoming wave packets.

Klein paradox, magnonic P-AP pair production. Further increasing the potential step above $2m$, for instance up to $B_z = 2$ T, we can temperarily have an effective energy overlap between the Ψ_+-state (particle) and the Ψ_--state (antiparticle) during the interaction at the edge of the potential step. As demonstrated in Fig. 3a by the micromagnetic simulations, P-AP (Ψ_+-Ψ_-) pair-creation processes are so triggered at the step edge by the incoming Ψ_+ magnons. More than 100%Ψ_+ magnons are reflected back and the Ψ_- magnons are spontaneously produced in the interior of $B_z = 2$ T, which resembles the results of quantum field theory showing that particles can be spontaneously produced in the presence of strong electric and gravitational fields[39,40]. Clearly, in magnonic systems Klein scattering is present, even though the SyAFM magnons possess a parabolic energy spectrum rather than a relativistic linear spectrum.

To further check the spontaneous pair production by strong magnetic fields, we consider a square potential barrier generated by the space-varying magnetic field: $B_z(x) = 2$ T, $1500 \leq x \leq 2000$ nm; and $B_z(x) = 0$, elsewhere. Indeed, Ψ_- magnons are generated and begin their oscillations in the barrier after first encounter of the Ψ_+ wave packet at the left barrier's edge. Subsequently, each reflection off the edge produces more Ψ_+-Ψ_- pairs and enhances the magnon densities inside the barrier, as shown in Fig. 3b (the barrier acts as the energy source).

Considering that $\Psi_{\pm}$ eigenmodes exhibit the charge-conjugation symmetry and the total circle-polarization charge is

conserved for a vanishing Gilbert damping, we can in this case describe the magnon tunneling across the potential step by defining the reflection and transmission coefficients as

$$R = \frac{\int \rho_r(x)dx}{\int \rho_i(x)dx} \text{ and } T = \frac{\int \rho_t(x)dx}{\int \rho_i(x)dx}, \qquad (11)$$

where ρ_i, ρ_r and ρ_t are the incoming, reflected, and the tunneling magnon densities at the step edge. The R and T of the incoming Ψ_+ wave packet with the center energy E scattered by the potential step B_z are numerically summarized in Fig. 3c: (i) Normal transmission with $R < 1$ and $0 < T < 1$ through a potential well when $B_z < (E - m)$; (ii) Perfect reflection with $R = 1$ and $T = 0$ when $(E - m) < B_z < (E + m)$; (iii) Anomalous Klein tunneling with $R > 1$ and $T < 0$ when $B_z > (E + m)$. The relation $R + T = 1$ does hold in all scattering cases. Notably, the supercritical Klein step gives rise to a sign reversal of the polarization-charge and momentum $\mathbf{k}$ of magnons inside the strong fields, thus resulting in negative transmission coefficient T. We should also note that T has a minimum (negative) value for the Klein tunneling of AFM magnons, which is different from the unbounded negative T in the quantum mechanical Dirac and Klein-Gordon wave packet dynamics (Supplementary Note 2)[24,27].

As pointed out by Schwinger[39], a spontaneous production of particles is closely related to the vacuum breakdown by a strong field. This process is non-perturbative. In our case nonlinear magnetic dynamics sets in when Gilbert damping $\alpha \neq 0$ is involved and at strong magnetic fields. As evidenced by N_z in Fig. 3d, in addition to the P-AP pairs generated by each interaction with the potential edge, the detailed simulations indicate that the density of Ψ_- magnons exponentially increases with traveling time inside the barrier because of the positive imaginary part of their energy due to the combined effect of strong field and nonzero damping. With such an increased density of circular-polarization (i.e., the transversal components of magnetization $|\mathbf{m}_n^\perp|$), the spin-flop transition is accelerated as well. The Néel ordering is then destabilized strongly and the AFM magnonic vacuum breaks down completely in the presence of the magnetic fields (see Supplementary Fig. 1).

Acausal transmission with negative tunneling time. A further aspect of the Klein paradox is the so-called "tunneling time problem"[41]. Following Feynman's picture of antiparticles as particle states moving backward in time[42], the P-AP pair production at the edge of the barrier hints on a negative tunneling time of incoming particles across a supercritical barrier. Here, we check this transmission mechanism based on the "physical" solution[43] by running simulations of chiral magnons in G-type AFMs, which have a linear energy spectrum and are less affected by the dynamic dipolar interactions (see Supplementary Note 3). The transmission process (simulation results are shown in Fig. 4) involves an emergent antiparticle wave packet $\Psi_-^{(1)}$ traveling forward in time from the left edge of the barrier. At this barrier edge and triggered by first encounter of the incoming particle wave packet $\Psi_+^{(1)}$, a P-AP pair production occurs. The wave packet $\Psi_-^{(1)}$ is then partially reflected back in the barrier into $\Psi_-^{(2)}$ and partially transmitted across the right edge to form the outgoing particle wave packet $\Psi_+^{(t)}$. Soon after, the antiparticle waves $\Psi_-^{(2)}$ are annihilated by the second incoming particle wave packet $\Psi_+^{(2)}$ at the left edge. Recall that an antiparticle wave Ψ_- going forward in time is equivalent to a particle wave Ψ_+ going backwards, we observe so an acausal process where the Ψ_+ magnon, scattered back into the past at the barrier's left edge, emerges from the barrier's right edge at an earlier moment. In other words, the Klein tunneling, $\Psi_+^{(2)} \rightarrow \Psi_-^{(2)} \rightarrow \Psi_+^{(t)}$ of AFM chiral magnons across the barrier demonstrates clearly a case of the acausal transmission mechanism.

Fig. 4 Acausal evolution of antiferromagnetic (AFM) magnons across the supercritical barrier. Red arrows point to the transmission pathway, $\Psi_+^{(2)} \rightarrow \Psi_-^{(2)} \rightarrow \Psi_+^{(t)}$ of the incoming $\Psi_+^{(2)}$ magnon within the Feynman's anti-particle picture. The corresponding magnon densities are quantified by the colour bar. A smooth Sauter potential is used during the simulations, where we have chosen $J = \hbar = \gamma = S = 1$. Other parameters are uniaxial magnetic anisotropy $\mathcal{K}_z = 10^{-4}$, Gilbert damping $\alpha = 10^{-5}$ and the lattice constant $a = 0.5$ nm.

Conclusion

The chiral magnons in AFMs associated with a breaking of anti-$\mathcal{PT}$ symmetry behaves qualitatively different from their FM counterpart. Right-handed and left-handed AFM magnon states at positive and negative energies are intimately interconnected and have to be described by spinor wavefunctions with the relative contribution of magnetic sublattices A and B, allowing to address anomalous tunneling problems such as the Klein paradox. Analytical and full-fledged numerical micromagnetic simulations show that the magnonic Klein paradox is related to the circular-polarization charge conjugation symmetry of the spinor wavefunctions, rather than the linear or parabolic energy spectrum of magnons in respectively G-type and synthetic AFMs. A locally applied strong magnetic field can bridge the chiral magnon gap, invert the polarization-charge carriers, and create antiparticle-like magnon states inside the potential barrier. Consequently, an incident particle-like magnon moving to the barrier can be scattered to a left-moving particle-like magnon state or a right-moving antiparticle-like magnon state. However, the scattering process does not alter the isospin state. The field-produced antiparticle-like magnons have positive imaginary eigen-frequencies enhancing exponentially the magnon creation in the barrier's interior. Such enhancement can be used to compensate for the density decay of traveling magnons which can be of relevance for chirality-dependent information processing and rectification of magnonic signals in magnonic circuits.

In principle, the tunneling anomalies are intrinsic properties of AFM chiral magnons and should be present in a wide class of materials. To be specific, we consider the FeCoB/Ru/FeCoB heterostructure as a prototypical SyAFM[32,33], in which the magneto-electric effects upon interfacing with ferroelectric materials allows for an electrical control of the RKKY interaction, magnetization damping, and the magnetic anisotropy, providing so a flexible way to investigate the Klein paradox. To further reduce the effect of magnetic dipole-dipole interactions from magnon dynamics, a G-type AFM waveguide made of, for instance FeO with the exchange coupling $J = 2.1$ meV and magnetic momentum $S = 3.5 \mu_B$, is suitable for focusing the transmission mechanism of exchange spin waves across the potential barrier. The magnetic fields of the order of 10 T can be effectively generated exploiting Helmholtz coil by placing locally two identical circular magnetic

coils on the up- and bottom-sides of AFM narrow strip. Furthermore, G-type AFMs are more robust against magnetic perturbations and have longer spin-flop time. So far, we studied the basic case of a flat space of the magnonic vacuum with less emphasis on non-linearities and many-body scattering. These regimes are readily realizable in AFM textures. This can be done for example, by involving spin-orbital-based effects on the magnons such as the Dzyaloshinsky-Moriya interaction and considering microscopically curved and/or topologically nontrivial structure of the AFM sample. Furthermore, our governing equations are extendable to capture the longitudinal spin dynamics and are inherently non-linear. The nonlinearities are controlled by magnetic damping and/or initial excitation amplitude. Magnon transport in structured AFMs is therefore a versatile platform to study basic physics problems and unravel new ways for using magnons in information transmission and processing.

Methods

Micromagnetic simulations of SyAFM dynamics. We use the Object Oriented MicroMagnetic Framework (OOMMF) for the numerical simulations of spin excitations in SyAFMs[44]. The SyAFM heterostructure is composed of two $(2500 \times 1 \times 1)$ nm³ FM wires with cell size of $(1 \times 1 \times 1)$nm³. The Gilbert damping $\alpha = 0.001$ and the gyromagnetic ratio $\gamma = 2.2 \times 10^5$ mA^{-1}s^{-1} are widely used in simulations of SyAFM dynamics, except in specially mentioned cases. Additional simulations based on the material parameters of CoFeB/Ru/CoFeB and (Pt/Co)$_2$/Ru/(Co/Pt)$_2$ multilayers show the same qualitative behavior as in the case of SyAFM dynamics.

Atomistic simulations of spin dynamics in G-type AFMs. For G-type AFMs, the simulations are performed by the open-source, atomistic and finite-difference micromagnetic solver Fidimag[45]. The coefficients to convert the external field B and time t to SI units are $\hat{t} = \hbar S/J$ and $\hat{B} = J/(\hbar \gamma S)$. Given that the AFM exchange coupling $J = 1$ meV and the atomic spin $S = 1$, we have then $\hat{t} \approx 0.66$ ps and $\hat{B} \approx 8.63$ T. The Sauter potential is given by a combination of two hyperbolic tangent field steps, $B(x) = B_z \left[\tanh(x - 2500)/25 - \tanh(x - 3000)/25 \right]/2$. The sharp-edge assumption is appropriate since the magnon wavelength is much larger the lattice constant a. The magnetic dipolar interactions are included for the antiferromagnetic environment.

Data availability

The data that support the findings presented in the main text and the Supplementary Information are available from the corresponding author upon reasonable request.

References

1. Goldstone, J., Salam, A. & Weinberg, S. Broken Symmetries. *Phys. Rev.* **127**, 965–970 (1962).
2. Strocchi, F. *Symmetry Breaking*, Lect. Notes Phys. 732 (Springer, Berlin, 2008).
3. Auerbach, A. *Interacting Electrons and Quantum Magnetism*. (Springer, Berlin, 1994).
4. Coey, J. M. D. & Parkin, S. S. P. *Handbook of Magnetism and Magnetic Materials*. (Springer, Switzerland, 2021).
5. El-Ganainy, R. et al. Non-Hermitian physics and PT symmetry. *Nat. Phys.* **14**, 11–19 (2018).
6. Stancil, D. D. & Prabhakar, A. *Spin Waves: Theory and Applications*. (Springer, New York, 2009).
7. Chumak, A. V., Vasyuchka, V. I., Serga, A. A. & Hillebrands, B. Magnon spintronics. *Nat. Phys.* **11**, 453–461 (2015).
8. Jungwirth, T., Marti, X., Wadley, P. & Wunderlich, J. Antiferromagnetic spintronics. *Nat. Nanotech.* **11**, 231–241 (2016).
9. Duine, R. A., Lee, K.-J., Parkin, S. S. P. & Stiles, M. D. Synthetic antiferromagnetic spintronics. *Nat. Phys.* **14**, 217–219 (2018).
10. Sui, C.-W., Yuan, S.-H., Wang, X.-G., Berakdar, J. & Jia, C. Emergent magnonic singularities in anti parity-time symmetric synthetic antiferromagnets. *New J. Phys.* **24**, 023031 (2022).
11. Keffer, F. & Kittel, C. Theory of antiferromagnetic resonance. *Phys. Rev.* **85**, 329–337 (1952).
12. Keffer, F., Kaplan, H. & Yafet, Y. Spin waves in ferromagnetic and antiferromagnetic materials. *Am. J. Phys.* **21**, 250–257 (1953).
13. Kim, C. et al. Distinct handedness of spin wave across the compensation temperatures of ferrimagnets. *Nat. Mater.* **19**, 980–985 (2020).
14. Jia, C., Chen, M., Schäffer, A. F. & Berakdar, J. Chiral logic computing with twisted antiferromagnetic magnon modes. *Npj Comput. Mater.* **7**, 101 (2021).
15. Liu, Y. et al. Switching magnon chirality in artificial ferrimagnet. *Nat Commun* **13**, 1264 (2022).
16. Barman, A. et al. The 2021 Magnonics Roadmap. *J. Phys.: Condens. Matter* **33**, 413001 (2021).
17. Yang, H., Wang, C., Yu, T., Cao, Y. & Yan, P. Antiferromagnetism emerging in a ferromagnet with gain. *Phys. Rev. Lett.* **121**, 197201 (2018).
18. Liu, H. et al. Observation of exceptional points in magnonic parity-time symmetry devices. *Sci. Adv.* **5**, eaax9144 (2019).
19. Tserkovnyak, Y. Exceptional points in dissipatively coupled spin dynamics. *Phys. Rev. Res.* **2**, 01303 (2020).
20. Wang, X.-G., Guo, G.-H. & Berakdar, J. Steering magnonic dynamics and permeability at exceptional points in a parity-time symmetric waveguide. *Nat. Commun.* **11**, 5663 (2020).
21. Wang, X.-G., Guo, G.-H. & Berakdar, J. Electric steering of spin excitation in nanostructured synthetic antiferromagnet. *Appl. Phys. Lett.* **117**, 242406 (2020).
22. Katsnelson, M. I., Novoselov, K. S. & Geim, A. K. Chiral tunneling and the Klein paradox in graphene. *Nat. Phys.* **2**, 620–625 (2006).
23. Dombey, N. & Calogeracos, A. Seventy years of the Klein paradox. *Phys. Reports* **315**, 41–58 (1999).
24. Calogeracos, A. & Dombey, N. History and physics of the Klein paradox. *Contemp. Phys.* **40**, 313–321 (1999).
25. Holstein, B. R. Strong field pair production. *Am. J. Phys.* **67**, 499–507 (1999).
26. Krekora, P., Su, Q. & Grobe, R. Klein Paradox in Spatial and Temporal Resolution. *Phys. Rev. Lett.* **92**, 040406 (2004).
27. Wagner, R. E., Ware, M. R., Su, Q. & Grobe, R. Bosonic analog of the Klein paradox. *Phys. Rev. A* **81**, 024101 (2010).
28. Wang, W., Gu, C., Zhou, Y. & Fangohr, H. Magnonic analog of relativistic Zitterbewegung in an antiferromagnetic spin chain. *Phys. Rev. B* **96**, 024430 (2017).
29. Gerritsma, R. et al. Quantum simulation of the Dirac equation. *Nature* **463**, 68–71 (2010).
30. Harms, J. S., Yuan, H. Y. & Duine, R. A. Enhanced Magnon Spin Current Using the Bosonic Klein Paradox. *Phys. Rev. Appl.* **18**, 064026 (2022).
31. Feynman, R. P. & Weinberg, S. *Elementary Particles and the Laws of Physics*. (Cambridge U. P., New York, 1987).
32. Yang, Q. et al. Ionic liquid gating control of RKKY interaction in FeCoB/Ru/FeCoB and (Pt/Co)$_2$/Ru/(Co/Pt)$_2$ multilayers. *Nat. Commun.* **9**, 991 (2018).
33. Wang, X. et al. E-field Control of the RKKY Interaction in FeCoB/Ru/FeCoB/PMN-PT (011) Multiferroic Heterostructures. *Adv. Mater.* **30**, 1803612 (2018).
34. Daniels, M. W., Cheng, R., Yu, W., Xiao, J. & Xiao, D. Nonabelian magnonics in antiferromagnets. *Phys. Rev. B* **98**, 134450 (2018).
35. Li, H.-F. Possible ground states and parallel magnetic-field-driven phase transitions of collinear antiferromagnets. *npj Comput. Mater.* **2**, 16032 (2016).
36. Bogdanov, A. N., Zhuravlev, A. V. & Rößler, U. K. Spin-flop transition in uniaxial antiferromagnets: Magnetic phases, reorientation effects, and multi-domain states. *Phys. Rev. B* **75**, 094425 (2007).
37. Böhm, B. et al. Antiferromagnetic domain wall control via surface spin flop in fully tunable synthetic antiferromagnets with perpendicular magnetic anisotropy. *Phys. Rev. B* **100**, 140411 (2019).
38. Kantner, C. L. S. et al. Determination of the spin-flip time in ferromagnetic SrRuO3 from time-resolved Kerr measurements. *Phys. Rev. B* **83**, 134432 (2011).
39. Schwinger, J. On Gauge Invariance and Vacuum Polarization. *Phys. Rev.* **82**, 664–679 (1951).
40. Hawking, S. W. Black hole explosions? *Nature* **248**, 30–31 (1974).
41. Ramos, R., Spierings, D., Racicot, I. & Steinberg, A. M. Measurement of the time spent by a tunnelling atom within the barrier region. *Nature* **583**, 529–532 (2020).
42. Holstein, B. R. Klein's paradox. *Am. J. Phys.* **66**, 507–512 (1998).
43. Gutiérrez de la Cal, X., Alkhateeb, M., Pons, M., Matzkin, A. & Sokolovski, D. Klein paradox for bosons, wave packets and negative tunnelling times. *Sci. Rep.* **10**, 19225 (2020).
44. Donahue, M. J. & Porter, D. G. OOMMF User's Guide, Version 1.0, NISTIR 6376 (National Institute of Standards and Technology, Gaithersburg, MD, 1999).
45. Bisotti, M.-A. et al. Fidimag - A Finite Difference Atomistic and Micromagnetic Simulation Package. *J. Open Res. Softw.* **6**, 22 (2018).

Author contributions

Funding

Competing interests

The authors declare no competing interests.

Additional information

Supplementary information The online version contains supplementary material available at https://doi.org/10.1038/s42005-023-01222-z.

Correspondence and requests for materials should be addressed to Jamal Berakdar or Chenglong Jia.

Peer review information *Communications Physics* thanks Olena Gomonay and the other, anonymous, reviewer(s) for their contribution to the peer review of this work. Peer reviewer reports are available.

Reprints and permission information is available at http://www.nature.com/reprints

Publisher's note Springer Nature remains neutral with regard to jurisdictional claims in published maps and institutional affiliations.